Acta Acustica 2024, **8**, 44

https://doi.org/10.1051/aacus/2024034

Topical Issue – Musical Acoustics: Latest Advances in Analytical, Numerical and Experimental Methods Tackling Complex Phenomena in Musical Instruments

Available online at: https://acta-acustica.edpsciences.org

SCIENTIFIC ARTICLE OPEN ACCESS

Assessing playability limits of bowed-string transients using experimental measurements

Alessio Lampis*, Alexander Mayer, and Vasileios Chatziioannou

Departments of Music Acoustics – IWK, University of Music and Performing Arts Vienna, Anton-von-Webern-Platz 1, Vienna 1030, Austria

Received 9 April 2024, Accepted 10 July 2024

Abstract – Understanding the dynamics of bowed-string attacks involves exploring the relationship between bow acceleration, bow force, and the generation of Helmholtz motion during transients. This study addresses the following research question: How do theoretical limits of "playability" predict these parameters? Motivated by the need for experimental evidence in this domain, we present a comprehensive investigation into bowed-string transients within the bow acceleration and bow force parameter space, known as the Guettler diagram. This study exclusively employs an experimental methodology. The setup, employing a robotic arm, permits the collection of transient data under varying bowing conditions. Analysis of the bridge force waveform allows for the extraction of pre-Helmholtz transient times. Our results reveal a triangular playable region in the Guettler diagram, consistent with theoretical predictions and previous experimental findings. However, Guettler's analytical limits for playable regions during transients show limitations. We investigate the role of friction, a key parameter idealized in the model used for obtaining these limits. Measured friction coefficients from transients reveal discrepancies with prior experimental studies, highlighting the need for further investigations in this direction.

Keywords: Music acoustics, Bowed string, Playability, Transients

1 Introduction

Bowed-string instrument musicians dedicate extensive practice time to refine their bowing technique in order to achieve the desired outcome. The players control the sound via three main parameters: bow velocity v_b, bow force F_b, and bow-bridge distance x_b. This work utilises the relative bow-bridge distance, denoted by β, which is defined as the ratio of the bow position x_b to the scale length of the string L.

There are certain limits in these parameters that must not be exceeded in a specific musical situation. Generally speaking, there are two situations in which the musicians might exceed the limits of "playability":

- when the bow force F_b they impress on the string is so small that the string's fundamental vibration fails, and we have a faint sound of the bow slipping on the string;
- when the bow force F_b is so large that the wave on the string is unable to trigger a clean repetition of periodic pulses with one stick and one slip per period and one single corner traveling along the string, i.e. Helmholtz motion, and we end up with a raucous sound.

Schelleng [1] examined the conditions required to maintain Helmholtz motion during steady-state and derived limits for the amount of force that a player may use before Helmholtz motion breaks down or an- other higher type of vibration takes place [2].

Further studies [3–8], consisting of both numerical simulations and experimental investigations, have been undertaken in recent decades to validate the limits proposed by Schelleng. These works have led to significant improvements, refining our understanding of the theoretical conditions necessary for sustaining Helmholtz motion. Notably, Woodhouse [9] has proposed a modified version of the minimum bow force that takes into account the instrument body resonances and torsional impedance of the string, which was compared to numerical simulations [10].

1.1 Playability in bowed attacks

A distinct aspect of bowed-string playability refers to the transient duration during attacks. While the Schelleng limits primarily address the maintenance of Helmholtz motion for sustained notes, playability during attacks is defined as the condition for achieving a "perfect" attack, that is, when the Helmholtz motion starts immediately after the initial string's slip [11]. Psychoacoustic studies [12] have demonstrated the perceptibility of short transient

*Corresponding author: lampis@mdw.ac.at

time before Helmholtz motion is developed, even of durations lasting hundredths of a second. These empirical findings suggest that transient durations within the range of 50–90 ms are generally perceived as musically acceptable by performers and listeners alike.

The exploration of string transients started with Raman's work [2]. Early work by Woodhouse [9] provided insight into the role of transients in determining playability. Later research by Schumacher and Woodhouse [13] revealed distinctions between sets of bow parameters in the creation of rapid transients. These systematic investigations used simulations to explore pre-Helmholtz transient durations, varying bow speed and force during the attack until reaching asymptotic values [13, 14]. However, their use of "switch-on" transients – artificial string excitations with non-zero bow force and speed at the onset – deviated from realistic musician-initiated bowing gestures.

An alternative method to "switch-on" transients was proposed by Guettler [11] who explored the use of bow force F_b and bow acceleration a as parameters for characterising transients in bowed strings: constant bow force at the attack start, with bow velocity gradually increasing from zero (constant acceleration a). Guettler's main observation was the correlation between the required bow force F_b and acceleration a for inducing "perfect" attacks when bowing at a fixed position along the string β. In particular, these parameters demonstrated a nearly proportional relationship. Nowadays, the prevailing method for illustrating the playability during bowed attacks involves plotting the transient time within a two-dimensional space defined by bow force F_b and bow acceleration a, commonly referred to as the Guettler diagram (see, e.g., Figs. 1 and 6).

1.1.1 Guettler's theoretical limits

Guettler derived analytical expressions formulating the constraints on bow force and bow acceleration necessary for achieving "perfect" attacks. His analysis led to upper and lower bounds of playability within the $F_b - a$ space. These bounds were derived from Guettler's examination of the friction force profile immediately following the first slip. The first slip refers to the relative motion that occurs between the string and the bow after the maximum friction force at the beginning of the attack is reached. For a comprehensive explanation of this analysis, refer to Guettler [11]. Here, we briefly outline the theoretical limits, maintaining the same nomenclature as in the original paper.

Assuming a simplified model of a perfectly elastic string (without stiffness), Guettler derived two conditions for the acceleration a constituting the upper and lower limits, represented as two inequalities. Referring to two waves sent from the bow contact point towards the nut and the bridge as "wave 1" and "wave 2," respectively, the first condition (condition A) requires that the bow should apply sufficient force against the string to generate a rising friction force before the first slip occurs, thereby preventing premature slipping before wave 1 reaches the bow from the nut. This condition translates into an upper limit for the bow acceleration:

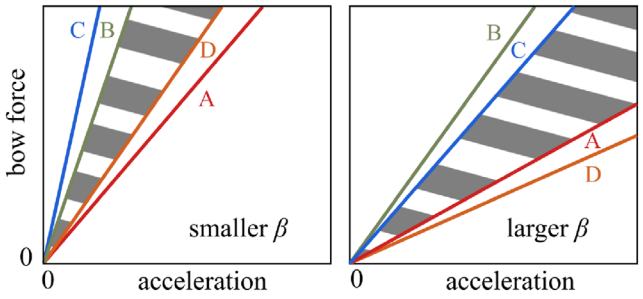

Figure 1. Two Guettler diagrams illustrating the theoretical limits for achieving "perfect" attacks. The solid lines represent the boundaries (conditions A–D) formulated by Guettler [11]. The bow acceleration should be maintained lower than both A and D, and higher than B and C. The influence of β is evident when comparing the two plots. For a smaller β (closer to the bridge), conditions B and D define the more stringent limitations for bow parameters. Conversely, for a larger β (further away from the bridge), conditions C and A become the more restrictive boundaries. The exact point at which these roles switch depends on the specific ratio between the dynamic and static friction coefficients.

$$\mathbf{A}: \quad a \le \beta(1-\beta)F_b[(3-4\beta)\mu_s - \mu_d - 2\sqrt{(1-2\beta)(2(1-\beta)\mu_s^2 - \mu_s\mu_d)}]/[(1-2\beta)TZ] \tag{1}$$

where μ_s is the static coefficient of friction, μ_d the dynamic coefficient of friction, T the string tension, and Z the string transversal impedance. The second condition (condition B) requires that the bow should apply an enough small force against the string to allow wave 2 to pass through the bowing point upon arrival from the nut, establishing a lower bound for the bow acceleration.

$$\mathbf{B}: \quad a > \beta(1-\beta)F_b \frac{3\mu_s - \mu_d - 2\sqrt{2\mu_s^2 - \mu_s\mu_d}}{TZ}. \tag{2}$$

Two additional conditions are necessary for sustaining Helmholtz motion. Guettler identified two instances in the time evolution of the friction force where Helmholtz motion could break down. Condition C requires that the wave 1 does not cancel out wave 2, after wave 1 catches up with wave 2 after $1/\beta$ periods. This yields a second lower limit:

$$\mathbf{C}: \quad a > \beta^2(1-\beta)F_b[(1-1.5\beta)(C+\lambda^{1/\beta})(\mu_s - \mu_{d1}) + \beta\mu_s - \sqrt{(2-3\beta^2)\left(C+\lambda^{1/\beta}\right)(\mu_s - \mu_{d1}) + \beta^2\mu_s^2}]/[2(1-1.5\beta)^2 TZ]. \tag{3}$$

Here, λ represents the reflection coefficient at the nut, μ_{d1} denotes the sliding coefficient of friction during the first slip, μ_{d2} the sliding coefficient of friction at the Helmholtz breakdown, and $C = (\mu_s - \mu_{d2})/(\mu_s - \mu_{d1})$. Moreover, Guettler's analysis points that the friction force occasionally reaches a substantial value after approximately $i(1-\beta)T_0$ time, with T_0 denoting the nominal period of oscillation

and i a coefficient ranging from 2 to 8 for $1/6 > \beta > 1/24$. The condition D requires that the bow must apply sufficient force against the string to prevent this increased friction force from inducing prematurely slipping. This results in a second upper limit for the bow force:

$$\mathbf{D}: a < \frac{F_\mathrm{b}\mu_\mathrm{s}}{TZ}\beta(1-\beta)\left[1-\beta+2i-3\beta i+\frac{\mu_\mathrm{d}}{\mu_\mathrm{s}}(1-\beta-2i+\beta i)\right.$$
$$\left.-2\sqrt{(1-\beta+\beta i)\left[2i-2\beta i+\frac{\mu_\mathrm{d}}{\mu_\mathrm{s}}(1-\beta-2i+\beta i)\right]}\right]\Big/$$
$$[(1-\beta-\beta i)(1-\beta-2i+\beta i)^2]. \quad (3)$$

Here, the determination of i is somewhat empirical. Guettler observed Helmholtz breakdown when $i = 1/(3\beta)$, see equation (12) in [11], although subsequent numerical studies suggested premature slip triggering at lower i [15].

The region within the $F - a$ plane satisfying these conditions forms a triangular wedge pointing towards the origin. This wedge arises from the intersection of conditions A and B, ensuring the initiation of Helmholtz motion from the first slip, and conditions C and D, ensuring its sustenance (see Fig. 1). In other words, for a given force, the acceleration must exceed both B and C while remaining below both A and D. When plotted for larger bow-bridge distances, the wedge widens and tilts clockwise.

It is important to note that these expressions are based on a series of assumptions regarding bow-string interaction and string dynamics. Namely, single-point bow-string contact, rigid bow hair, and rigid string terminations with small losses are assumed, while string torsion, dispersion, and the effect of temperature on rosin are neglected. Additionally, the requirement for the bowing point $1/\beta$ to be an integer is imposed.

Guettler's numerical simulations, incorporating these assumptions, align reasonably well with the analytical limits. By systematically varying bow force and bow acceleration in time-domain simulations and plotting transient time for each parameter set, Guettler constructed a playability map in the parameter space $F_\mathrm{b} - a$ to visualise the playable region and compare it with analytical limits [11]. Subsequent comparisons also showed similar agreements using a non-stiff string model in simulations [15]. Condition C was found to have negligible impact on numerical simulations by Guettler, except for the largest β, a finding confirmed in [15]. Although these conditions themselves may not directly apply to more realistic systems, they offer insight into the conditions necessary for Helmholtz motion development.

1.2 Previous measurements of Guettler diagrams

The only Guettler diagram derived from experimental data is attributed to Galluzzo [5]. Employing a bowing apparatus, his work revealed that within the $F_\mathrm{b} - a$ space, a triangular region consisting of playable transients (Helmholtz motion within a 20-period duration) emerges.

Furthermore, he observed a "speckled" pattern of transients, similar to those recognised in numerical simulations utilising complex models [16]. This pattern appears as a location of "perfect" attacks and failed transients within the playable region next to each other, with variability apparent across measurements. Exhaustive testing with a bowing machine demonstrated a degree of repeatability in results, but limited by the chaotic nature of transients. Consequently, it was inferred that achieving "perfect" transients under identical nominal conditions, particularly near the limits of the wedge, is improbable.

Nevertheless, a proportional relationship between the upper and lower limits of bow force and the force itself was observed, despite the "blurred" borders of the triangle region. To delineate a more reliable region, measurements were repeated 12 times, identifying areas leading to rapidly established Helmholtz motion. Further insights from his work are reported in detail in [5].

1.3 Aim of the study

The primary goal of the present study is to experimentally investigate the limits of bow force F_b and bow acceleration a within the Guettler diagram.

This research explores the playability constraints during bowed-string attacks, employing experimental data and comparing the findings with existing literature. The central question motivating this study revolves around the use of friction coefficients, extracted from the transient waveform of the bridge force, as a modifying factor for the analytical expressions originally proposed by Guettler. Recognising that Guettler's limits are overly idealised to align with experimental results, they nonetheless serve as the only analytical framework for predicting regions leading to "perfect" Helmholtz motion attacks. Thus, it is important to determine whether these theoretical limits may be informed by experimental observations.

The only work [5] incorporating experimental data to construct a Guettler diagram revealed intriguing aspects of transient time behaviour not previously observed in numerical studies [16]. These observations were done by repeated measurements, parameter space scanning in reverse order, and varying the bow position along the string. These approaches were replicated in the current study. Differently from Galluzzo's setup, which utilised a D-string mounted on a cello for data acquisition, our experiments employed a G-string mounted on rigid terminations in a monochord configuration to mitigate vibrational influences from the instrument's resonance modes. Previous investigations encompassed a comparison of results obtained using a perspex rod as an exciter and an actual bow, yielding similar results. Consequently, we opted to limit string excitation to an actual bow.

2 Method

The experimental data for constructing the Guettler diagrams were collected with an apparatus consisting of a single cello string mounted on rigid terminations, and a robotic arm (UR5e by Universal Robots) for string excitation, both installed on a heavy optical table. The two rigid

terminations are referred to as the "bridge" and the "nut". On the bridge, the string is supported by a sensor capturing the string force on the transversal plane. Such a bridge sensor measures the static and dynamic force, since it is constituted by load cells [17]. On the flange of the robotic arm, a self-made end-effector is installed. This serves for measuring the bow force and holding the bow. A thorough explanation of the whole apparatus is provided in a technical report [18].

Signals are acquired through a data acquisition card connected to a PC. For this study, the nut, and bridge force signals, the string tension, the bow force, and the robot coordinates are simultaneously recorded at a 50 kHz sampling rate. The experimental setup is situated at the laboratory of the Department of Music Acoustics (IWK) of the University of Music and Performing Arts Vienna. A photo of the main components of the setup is provided in Figure 2.

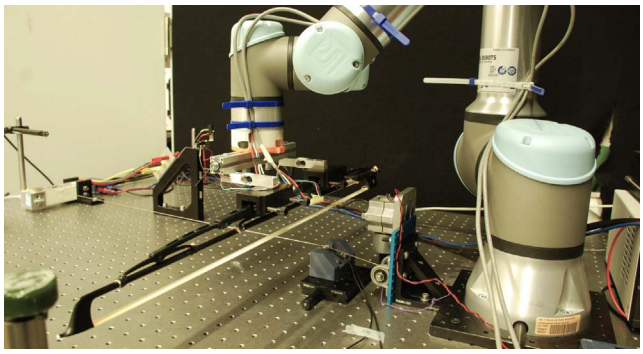

Figure 2. Photo of the experimental setup. A robotic arm (left) holds a bow exciting a cello string (centre). The two string terminations, the "bridge" (closer to the robot) and the "nut" (further away), are visible. The entire setup is mounted on an optical table for stability and vibration isolation.

2.1 String excitation

For each bow stroke, acceleration and bow force change by changing the robot's motion settings, and are recorded along with the string force at the bridge. The robot coordinates and force signals are processed to extract the string excitation conditions that appear as coordinates in the Guettler diagram.

It was noted that tensioning the bow hair above the typical playing conditions resulted in a more stable force, specifically in the area around the middle of the bow. For this reason, it was found to be sufficient to over-tension the bow hair to ensure an almost constant bow force along the desired bow journey. In this way, no automatic force control, as the ones present in other bowing machines [19, 20], was required. It was sufficient to keep the bowing area to a length of 6 cm in the middle of the bow hair. Oscillations of the bow force were carefully tracked and reported in Section 2.2. For this study, a student bow (Artino Cello Bow 4/4 Special Edition) in which the stick is made of fibreglass was used. The rosin employed was a J100M Jade L'Opera, suitable for violin, viola, and cello.

We controlled the kinematics of the bow movements, such as its position, velocity, and acceleration, using the robotic arm. A program was designed in the commercial software of the robotic arm (PolyScope) in order to perform strokes with controlled parameters. Moreover, the program interfaces the robot with the recording software [21], in order to trigger recordings starts and stops, while sending the robot coordinates to be recorded.

To scan the $F_b - a$ space, the robot performs a series of commands that result in the following bow movements: the bow hair is pushed against the string, then the bow is moved perpendicularly to the string, in a linear trajectory and with constant acceleration until a distance of 6 cm, after which the bow decelerates. The robot then moves the bow to the starting position, and the program instructs to increase the acceleration of the stroke by 0.1 ms^{-2}. When the acceleration reaches the final value of 3.15 ms^{-2}, the robot changes its vertical coordinate, going down by a step of 0.2 mm thus increasing the force with which the bow hair are pushing against the string. This results in a slight increase of the bow force. When the measurements are done in reverse order, the starting point corresponds to the maximum force and maximum acceleration, then at each cycle the acceleration decreases with the same step.

In practice, the bow force was not directly controlled. The elevation of the bow with respect to the string results in having different bow forces. The goal was to span a wide range of bow forces, so the choice of bow elevations would cover a span of about 1–3 N.

The bow speed is retrieved from the coordinates of the robot's tool flange position. From the velocity profile, the acceleration is computed from its slope. An example of the bow velocity profile (and the relative acceleration) and the bow force is shown in Figure 3.

A commercially available cello G-string from Thomastik-Infeld (Dominant, medium gauge) was used for these experiments. The string has a synthetic core and chrome winding. Detailed information on the string's properties is presented in Table 1.

The string tension T was directly measured using a dedicated load cell. The fundamental frequency f_0, the bending stiffness B and the quality factor Q were derived from the string's pluck response, employing the wire breaking method. The plucking was repeated three times, and the mean values and standard deviation is reported in Table 1 and Figure 4.

It is important to note that the string properties reported in Table 1 and Figure 4 were measured after the first measurement session (see Sect. 3.1). This involved mounting the string and allowing it to adapt to the tuning tension for several days before collecting the data. As observed in Table 1, the measured fundamental frequency (97.8 Hz) deviates slightly from the expected G note (98 Hz). This discrepancy can be attributed to the detuning of the string after multiple bowings during the measurement session.

By analysing the inharmonicity of the string natural frequencies across transverse modes, it is possible to determine B [22]. The theoretical quadratic relationship between

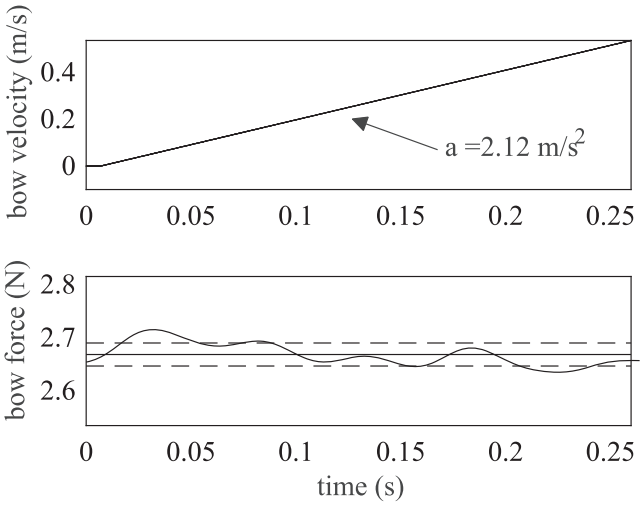

Figure 3. An example of bow velocity and bow force measured signals during an attack. The acceleration a is derived from the slope of the velocity profile. The bow force used for the Guettler diagram corresponds to the mean of the bow force signal during the transient (horizontal line in the bottom plot). The dashed lines in the bottom plots represent the standard deviation of the bow force.

the natural frequency normalized by the mode number f_n/n and the mode number n is expressed as $f_n/n \approx a + cn^2$, with $B \approx (2cTL^2)/(a\pi^2)$ [23]. The best fit to the measured normalised frequencies permits to estimate B, and it is represented by the dashed line in Figure 4a.

The damping characteristics of the first 30 modes were measured alongside the inharmonicity. The Q factor is calculated for each mode as the ratio between the natural frequency and the bandwith of the -3 dB drop of the power spectra around the natural frequency. The results are presented in Figure 4b, with the dashed line representing the best fit of the Valette model for frequency-dependent damping [24]. For both plots in Figure 4b, the missing data points correspond to modes that were not efficiently excited due to the plucking position (same β referred in Sect. 3.1). Error bars indicate the standard deviation of the measurements for three plucks.

2.2 Performance of the apparatus and experimental conditions

We evaluated several factors influencing the system's performance to ensure experimental robustness and repeatability. These factors include variation in string properties, bow force and acceleration fluctuations during attacks, and environmental conditions throughout the experiments. The string properties were assessed by measuring variations between different experimental sessions.

The bow force during the attack exhibits slight oscillations, as illustrated in Figure 3. However, the magnitude of these variations is minimal and comparable to previous studies [19]. The standard deviation of the force profile for each attack quantifies these oscillations (see dotted line in Figure 3). The maximum standard deviation across all recordings was 0.0667 N, with an average deviation of 0.05 N. Notably, this deviation tends to increase with higher force and acceleration values.

Table 1. Measured and derived properties for a Thomastik Infeld Dominant G cello string mounted on rigid supports. Values of the tension T and the frequency f_0 were measured right after the first measurement session (Sect. 3.1). Three plucked-string signals were obtained by wire-breaking method after the measurement session to measure the bending stiffness B and the quality factor Q as a function of frequency (see Fig. 4).

Parameter	Value	Unit	Note
Tension T	116.1	N	Measured
Scale length L	0.7	m	Measured
Diameter d	1.15	mm	Measured
Frequency f_0	97.86	Hz	Measured
Linear density μ	6.2	g/m	$\mu = \mathrm{T}/(2Lf_0)^2$
Impedance Z	0.849	Kg/s	$Z = \sqrt{\mu T}$
Bending stiffness B	3.03 ± 0.015	10^{-4} N m^2	Measured

Measurements of bow acceleration deviated slightly from the nominal values programmed in the robotic arm software, particularly above 2 ms^{-2}. This could be attributed to limitations of the robotic arm at high velocities or the method of extracting velocity from position data. Typical values for the deviation were 0.01 ms^{-2} for accelerations up to 2 ms^{-2} and 0.1 ms^{-2} for accelerations up to 3.15 ms^{-2}.

String tension naturally decreases with playing time. In our experiments, the string was tuned at the beginning of each session, and tension changes were monitored throughout. Typically, the string loss in tension was by 0.7 N, with a maximum observed of 1.45 N.

Environmental conditions were monitored throughout the experiments by continuously recording temperature and humidity. The average temperature during the measurements presented in this paper was 22 °C. However, some temperature fluctuations of about 1 °C were observed within each measurement session used to generate a single Guettler diagram. Humidity fluctuations were generally minimal during measurement sessions.

2.3 Detection of transient time

Since distinct vibration regimes of a bowed-string result in characteristic waveforms of the bridge force signal, these signals are commonly used to categorize the string's vibrational regimes. This work employs an automatic classification detection algorithm used also for computing transient time, originally proposed by Woodhouse [25] and further developed by Galluzzo [5]. The algorithm relies on detrending the bridge force signal to resemble a step function. Subsequently, the distances between histogram peaks of the detrended signal provide an indication of the durations between consequent stick phases. The interval between consecutive peaks is compared to the theoretical "flyback" amplitude of Helmholtz motion. If the difference is negligible, the specific segment is classified as Helmholtz motion (see Fig. 5).

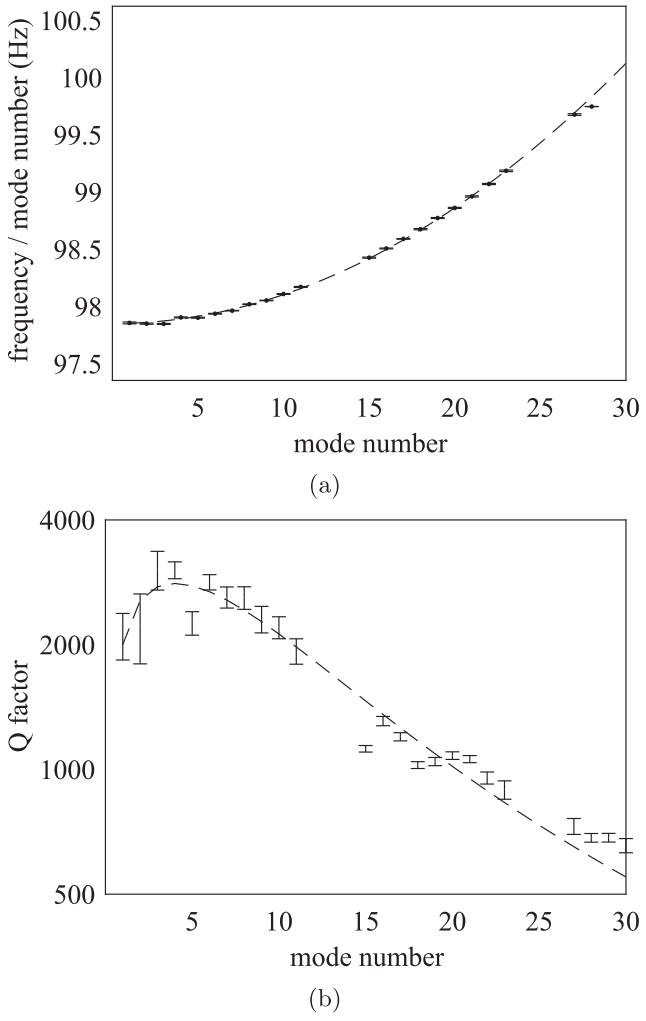

Figure 4. (a) The natural frequencies of a Thomastik Infeld Dominant G cello string normalised by the mode number across transverse modes. The dashed line represents the best fit of a theoretical quadratic relationship. (b) The Q factors as a function of the same modes. The dashed line represents the best fit of the Valette model for frequency-dependent damping.

The pre-Helmholtz transient duration is calculated from the time of the first slip to the first instance of sustained Helmholtz motion. To ensure reliable detection of sustained Helmholtz motion, we required its identification in three consecutive instances. This method might be more effective for assessing sustained behaviour in shorter signals, while longer signals might exhibit extended periods of Helmholtz motion followed by a breakdown only near the signal's end. However, given the limited bow region employed in this study compared to typical playing conditions, this method remains appropriate.

A separate algorithm was implemented for first-slip detection, as the method in [5] can exhibit instabilities at very low bow velocities, leading to an "exploding" detrended function. Our alternative approach involved calculating the derivative of the bridge force signal, which generates pulses corresponding to the slip phases. By simply identifying the first pulse, the moment of first slip could be determined. While this method is less robust for scenarios lacking a clear first slip (a challenge for most detection algorithms), it avoids potential issues encountered with the method in [5] at low velocities.

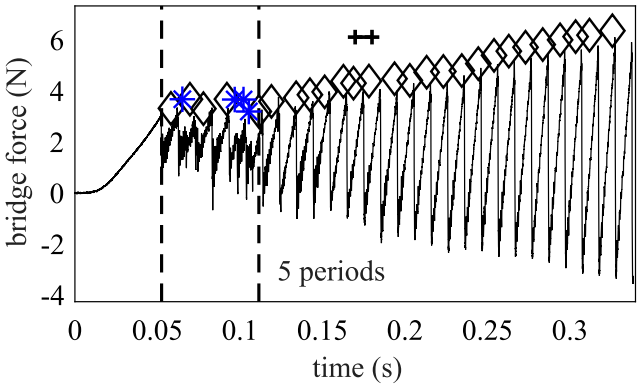

Figure 5. An example of the detection algorithm used for identifying vibration regimes in the bridge force signal and computing the pre-Helmholtz transient duration. Helmholtz motions are marked with diamonds "◇", multiple slips with blue asterisks "*". The marker on the top "++" serves as a reference for the duration of the nominal vibration period.

To facilitate Helmholtz motion detection, signals with a fundamental frequency exceeding twice the string's nominal frequency were labelled as failed transients. However, this approach was insufficient to eliminate all S-motion regimes, as these can also exhibit a dominant frequency at the string's nominal frequency. Therefore, we computed the zero-crossing rate (ZCR) within a 0.2 s window following the first slip, normalised by the nominal vibration period. Signals with a ZCR > 3 in this time window were labelled as failed transients.

3 Experimental Guettler diagrams

3.1 Results at one value for β

A Guettler diagram was obtained for the G-string on the monochord with 30 values of a, 33 values of F_b and at the relative bowing position of $\beta = 0.0786$. The pre-Helmholtz transient time is plotted as a function of a and F_b, as shown in Figure 6. The scattered points are coloured according to the transient time. Black points represent failed transients, i.e. with a detected time equal to or bigger than 20 periods, while white points represent "perfect" attacks with 0 periods duration. Bow strokes with varying a were performed for each force. For this measurement, F_b and a were varied in ascending order. The duration of pre-Helmholtz motion was computed automatically by the detection algorithm described in Section 2.3. Following Galluzzo [5], the transient was considered successful if the duration between the first slip and sustained Helmholtz motion was less than 20 periods time, corresponding to 0.204 s. In our case, we considered sustained Helmholtz motion if it was detected for at least three consecutive

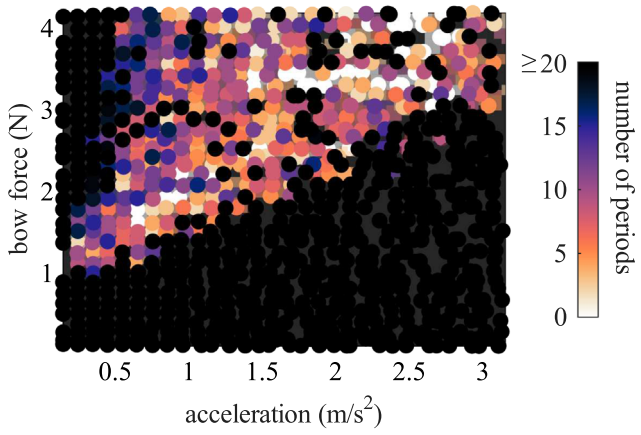

Figure 6. Guettler diagram for a Thomastik Infeld Domainant G cello string mounted on rigid supports at a relative bow-bridge distance β= 0.0786. The pre-Helmholtz transient duration is given by the colour of each point at a certain combination of bow force F_b and bow acceleration a. White points indicate an immediate onset of the Helmholtz motion, while black points indicate failed transients (duration of 20 period lengths or more).

occurrences at the end of the signal. A manual inspection was performed for 50 detected waveforms, focusing on the borders of the playable region, in order to assess the accuracy of the detection. Occasionally, motions with multiple flyback [19] were misidentified as Helmholtz motion, and labelled as failed transients by the experimenter. Looking at Figure 6, it can be noted that the data points are not aligned on a perfect grid, especially for acceleration values higher than 2 ms^{-2}.

The triangular shape of the playable region is in agreement with Guettler's predictions [11]. The upper and lower limits form approximately straight lines. However, differently from conditions A–D, the borders do not point towards the origin, as there is a non-playable area below the bow force of around 1 N. Inside the playable region, there are occurrences of failed transients, showing similar speckled patterns as observed in previous experimental data [5]. There is not a clear area where "perfect" transients are gathered. The diagrams from both Galluzzo and our study exhibit the absence of radial lines with seemingly identical transient time, that are instead present often when using numerical simulations [16].

While one single Guettler diagram provides insights into playability limits, further investigation is needed to confirm the validity of these observations. The next section presents results from six repeated measurements with varying measurement order and string conditions. This extended dataset will shed light on the potential variability or the chaotic nature of transients.

3.2 Reproducibility of the measurements

To assess the repeatability and robustness of the observed playable region and transient behaviour, we conducted five additional measurements with varying order and at one month distance. This aimed at isolating potential systematic effects arising from changes during the measurement session, such as rosin depletion, string tension variation, and bow hair tension changes.

The first four repetitions alternated between the original ascending order and reversed order within a day distance. This design allowed us to identify any order-dependent influences on the results. For example, as the rosin is applied at the beginning of the session, one might argue that more rosin is available initially. Additionally, string tension naturally detune after extended playing, and bow hair tension might also decrease during the measurement. These factors can potentially influence the playable region and transient times.

Furthermore, de-tensioning and re-tensioning processes could potentially influence string properties, which in turn might affect bow-string interaction. To investigate the long-term stability and impact of string ageing on playability limits, two further repetitions were conducted one month later after dismounting and remounting the string.

Figure 7 presents the repeated Guettler diagrams. Due to varying bow force ranges across repetitions, all diagrams were cropped for consistent comparison while retaining sufficient data points for analysis. Features like playable region shape, size, and distribution of "perfect" transients were analysed for each repetition. Overall, the playable region size and shape remained consistent across all repetitions, regardless of measurement order or string condition. Moreover, it is important to note that the 1 N lower force limit was observed in other repetitions where data below 1 N were available, even though it is not directly visible in Figure 7 due to cropped force ranges. Interestingly, this unplayable region at 1 N was also observed in other measurements using different string types, with both ascending and descending order. These additional data are not included in this paper.

A minor difference was observed in the last repetition (right bottom of Fig. 7), where the right side acceleration limit deviated slightly from an apparent straight line seen in other plots. It is yet unclear if this behaviour is caused by a systematic change in system parameters or is due to random variations.

Figure 8 displays the averaged transient time across repetitions. The data points from each repetition were not identical, so we used an interpolated grid (100 × 100 points) to create this averaged representation. For each grid point within the map, the average transient time was calculated by taking the mean value across all repetitions. This analysis identified a "brighter" region in the map, which corresponds to a zone where the pre-Helmholtz transient time is shorter. Other than this aspect, the repeated measurements largely confirm the initial findings from Figure 6, suggesting consistent Guettler limits and transient time distribution within the playable region (see also Sect. 4).

3.3 Results at different β

Following the results at a fixed string position (β = 0.0786), we further investigated the influence of β by making measurements at four distinct positions along

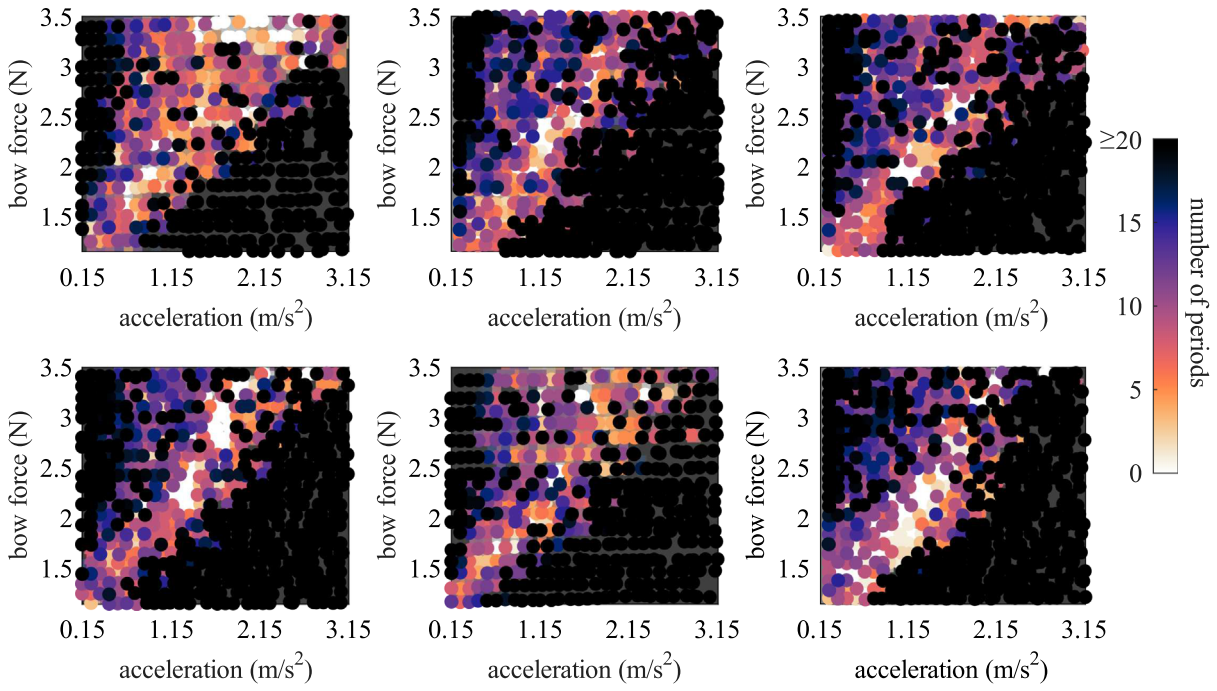

Figure 7. Six repetitions of the Guettler diagram. To facilitate visual comparison across plots, the y-axis has been cropped to accommodate the same force values in each plot. The top-left plot is identical to Figure 6 and serves as a reference. The remaining plots depict Guettler diagrams acquired by systematically varying bowing parameters in either ascending (top row) or descending (bottom row) order during the measurement sessions. The left and centre columns show results obtained on consecutive days without removing the string from the apparatus. The rightmost column displays Guettler diagrams measured after a one-month interval, with the string having been dismounted and remounted in the meantime.

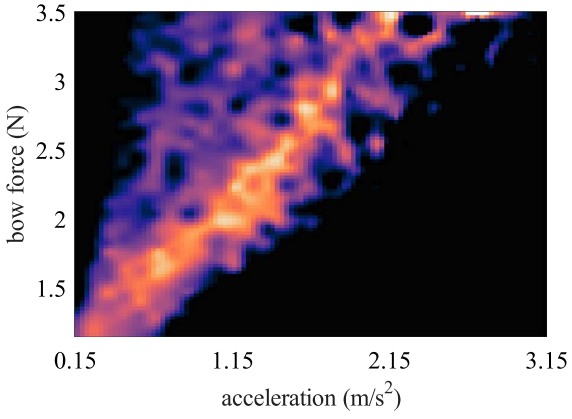

Figure 8. Average pre-Helmholtz transient time across the six repetitions shown in Figure 7. To create this visualisation, each of the six individual Guettler diagrams was first interpolated onto a common grid with 100 rows and 100 columns. Following interpolation, the average transient time was calculated for each grid point by taking the mean value across all repetitions. The observed "brighter" region represents a zone where the bow-string interaction generally leads to shorter pre-Helmholtz transient times.

the string: $\beta = 0.0429$, 0.0786, 0.121, and 0.164. These positions were chosen to minimise the occurrence of S-motions, known to appear at integer ratios of the string's playable length. Notably, the position at $\beta = 0.0786$ coincides with the one used previously, and therefore is used as an additional repetition.

As expected from the current literature, the playable region rotates clockwise in the Guettler diagrams with increasing β (see Fig. 9).

An intriguing observation from Figure 9 is the significantly higher "brightness" of plots at higher β. This shows a very limited number of transient times falling within the 5–20 period range. This suggests that at lower β, i.e. playing closer to the bridge, phenomena may exist that disrupt the periodic triggering of slips during the attack's initial phase. Furthermore, the boundaries of the playable regions in the latest plots ($\beta = 0.121$ and 0.164) appear more scattered and deviate from straight lines compared to $\beta = 0.0786$. These observations could also be partially attributed to the exclusion of S-motion during the detection phase.

In conclusion, these results compared our experimentally derived Guettler diagrams with previous studies [5] using similar approaches. While confirming the general behaviour of Guettler diagrams, we observed minor deviations from the existing literature. The next section will explore an alternative comparison, utilising the experimental data to assess the deviation between the theoretical Guettler limits and the experimentally determined playability limits.

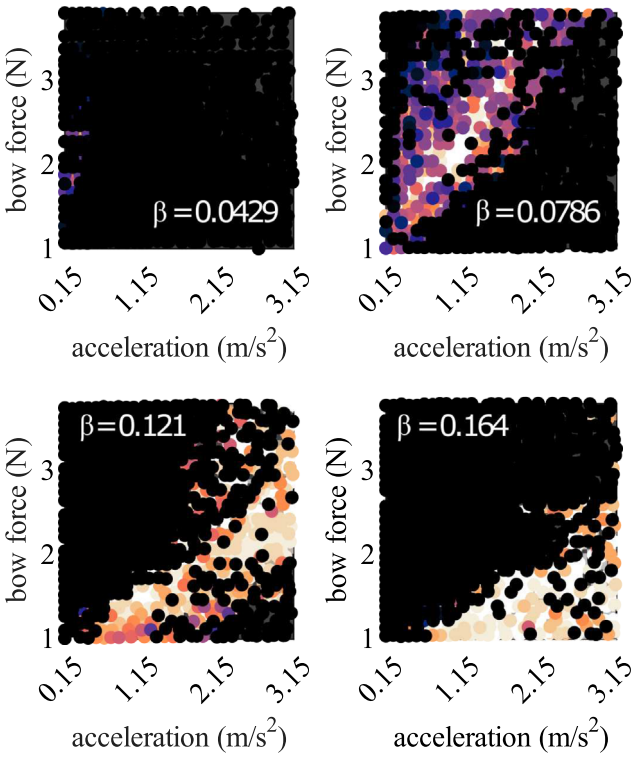

Figure 9. Guettler diagrams at different string positions β. As expected, the playable region rotates clockwise with increasing β. Higher β values exhibit smaller transient times within the 5-20 period range. Compared to $\beta = 0.0786$, the latest plots show more scattered playable region boundaries.

4 Comparison with Guettler limits

This section compares the theoretical limits derived from conditions A–D with the experimentally observed playable region in the Guettler diagram. It is important to note that our Guettler diagram includes transients longer than zero period duration, while the analytical analysis of Guettler considers "perfect" attacks only. Moreover, deviations from the theoretical limits are expected due to idealised assumptions.

Figure 10 utilises the Guettler diagram from Section 3.1 as the basis for comparison with the analytically derived Guettler limits. Specifically, Figure 10a displays the duration between the first slip and the first occurrence of detected Helmholtz motion, i.e. two consecutive stick phases per period, regardless of whether this motion is sustained. In contrast, Figure 10b repeats the same information presented in Figure 6 by showing the duration between the first slip and the first occurrence of sustained Helmholtz motion. To accommodate the visualisation of multiple lines overlaid on the same plot in Figures 10a and 10b different colour scheme is employed compared to Figure 6. Examining Figures 10a and 10b reveals that some transients may start with initial parts classified as Helmholtz motion (appearing as bright spots in Fig. 10a). However, this motion might not last throughout the entire transient. Figure 10b shows most of these same transients lasting longer, suggesting that Helmholtz motion is not sustained.

String tension and transverse impedance were obtained from measured string properties, while the nut reflection coefficient ($\lambda = 0.998$) was derived from the measured pluck response at the nut. Our study employs constant friction coefficients for simplicity, whereas previous works incorporated small variations in friction coefficients during simulations to compute conditions A–D [11, 15]. These variations were observed to be minimal when using the hyperbolic friction model. In contrast, we did not use any friction model to inform the limits with friction coefficients. Given the high sensitivity of the Guettler inequalities to friction coefficients, two sets of friction coefficients were employed. The values selected were chosen to resemble those commonly employed in literature (for instance, [26]). The resulting limits are displayed in Figure 10, with continuous lines representing conditions obtained using ($\mu_s = 1$, $\mu_d = 0.5$, $\mu_{d1} = 0.4$, $\mu_{d2} = 0.3$) and dotted lines representing those obtained with ($\mu_s = 0.8$, $\mu_d = 0.3$, $\mu_{d1} = 0.2$, $\mu_{d2} = 0.1$). While these sets of coefficients are similar, noticeable variations can be observed in conditions A, B, and C.

By only focusing on the transient time after the first slip, without considering the subsequent maintenance of Helmholtz motion, we can better assess the string behaviour described by conditions A and B. These conditions aim to predict "perfect" attacks after the first slip, not the continuation of Helmholtz motion.

This approach aligns with Demoucron's observation that considering only the initial triggering, leads to better agreement with simulations of flexible strings [15]. Figure 10a reveals limitations in conditions A and B for identifying the "perfect" attacks region (0-1 period length) during the initial triggering phase.

Conversely, conditions C and D are better suited for describing the region where Helmholtz motion is maintained. Therefore, these conditions should be compared to the Guettler diagram in Figure 6. Condition D additionally depends on the ratio μ_d/μ_s [11]. For example, for $\mu_d/\mu_s = 0.5$, condition A becomes more restrictive when $\beta > 1/6$. However, in our case with $\beta < 1/6$, the maximum acceleration predicted by condition D (as seen in Fig. 10b) proves more restrictive when $i = 1/(3\beta)$, as suggested by Guettler. To align the boundary of condition D with the higher limits in our experimental diagram, a bigger normalised period index $i\beta = 0.667$, corresponding to $i = 1/(1.5\beta)$, was empirically found. The resulting line is displayed in Figure 10b and labelled as D*. Figure 10b builds upon Figure 6 by overlaying the "perfect" attacks (0-1 period length) onto the Guettler diagram. This visualisation effectively highlights that conditions C and D delineate a clear playable zone where "perfect" transients are more likely.

This comparison reveals that the Guettler conditions are not entirely suitable for determining the extent of the experimental playable region. This highlights the need for further investigation into how the Guettler limits can be physically informed. Notably, the only parameters

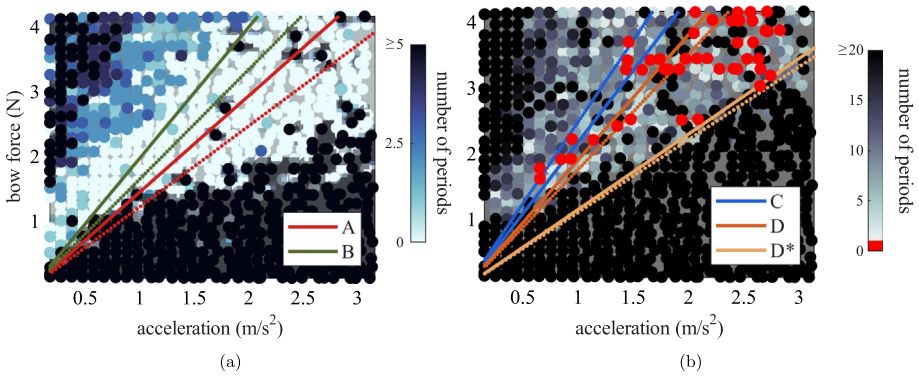

Figure 10. Comparison between Guettler theoretical limits and measured transient times in the Guettler diagram from Section 3.1. In (a) the plot displays the duration between the first slip and the first instance of Helmholtz motion regardless of whether this motion is sustained. Conditions A and B are overlaid on the plot (solid and dashed lines). Two sets of friction coefficients are used to illustrate their influence on these conditions. The dotted lines represent the conditions computed with lower friction coefficients compared to the solid lines. In (b) the transient time is displayed as in Figure 6, but uses a colour scheme optimised for displaying multiple lines. Here, "perfect" transients (lasting 0-1 period length) are highlighted in red. Notably, these "perfect" transients fall largely within the region bounded by conditions C and D*.

not directly extracted from the actual string were the friction coefficients. Static and dynamic friction coefficients can be estimated from the bridge force and bowing parameters [5].

4.1 Friction coefficients in the Guettler space

This section describes the approach used to derive friction coefficients from measured data, which will then be utilised in the analytical Guettler limits. Instead of relying on literature values, we employ friction coefficients extracted from the bridge force signal for each Guettler diagram point in Figure 6.

The static friction coefficient μ_s is estimated through a simple equilibrium analysis of the bridge force. The assumption is that μ_s is proportional to the maximum force just before the initial slip. The bridge force signal is subjected to an angular transformation to isolate the force component acting perpendicular to the bowing direction. Assuming a constant ratio between the bridge force and perpendicular force throughout the string length (due to quasi-static forces before the first slip), the ratio at the bridge is assumed equivalent to the contact point's force ratio, yielding the static coefficient. This calculation is performed for each bridge force signal associated with each Guettler diagram point. The results, shown in Figure 11a (top plot), differ from Galluzzo's observations [5, 16]. Our average μ_s across all measurements (including repetitions and varying β) is approximately 1.4, contrasting with Galluzzo's average of 0.66. Our μ_s exhibits strong dependence on bow force but minimal dependence on bow acceleration. We have also calculated μ_s using the same procedure as Galluzzo, dividing the bridge force just before first slip by $(1 - \beta)F_b$ [5], to exclude possible influence from the data analysis. Despite this difference, both methods yielded practically identical trends and mean values of μ_s. To improve the representation of the friction coefficients μ, a second-order polynomial curve is fitted to the data

$$\mu \approx x_0 + x_1 a + x_2 F_b + x_{12} a F_b + x_{11} a^2 + x_{22} F_b^2. \quad (5)$$

This quadratic fit, shown in the bottom plots of Figure 11, performs better than a linear fit (minimising the sum of squared errors). Outliers are removed based on median absolute deviation criteria before fitting. The values of the fitting coefficients are collected in Table 2.

Based on the observation in [5, 27] that the bridge force jump at the first slip relates to friction coefficient change, μ_{d1} is computed by subtracting the change in friction coefficient from μ_s. The measurements of μ_{d1} and the fitted curve are displayed in Figure 11b. The trend resembles that of μ_s, with the difference between static and dynamic coefficients increasing from 0.6 at lower bow forces to 1 at higher forces.

Deriving μ_{d2}, the friction coefficient at the Helmholtz motion breakdown point, presents complications. Instead of precisely tracking the slip, the static and dynamic friction coefficient at the second slip is measured, similarly to μ_s and μ_{d1}, respectively. The jump in friction coefficient at this second slip is then used to estimate μ_{d2}. This approach acknowledges that the actual friction coefficient at the breaking point might be lower. This is because as the relative bow-string velocity increases, the dynamic coefficient typically decreases. Consequently, a significant drop in the dynamic coefficient may occur during the attack after the first slip. For deriving μ_d, an "averaged" dynamic friction coefficient is employed. This value represents the ratio between the average bridge force in the bowing plane and the average bridge force in the perpendicular plane. The assumption is that the quasi-static component of the bridge force is proportional to the average friction force at the bowing point. The average window is chosen to be 0.1 s, which corresponds to a typical development time for Helmholtz motion. The plots in Figure 11c reveal discrepancies between

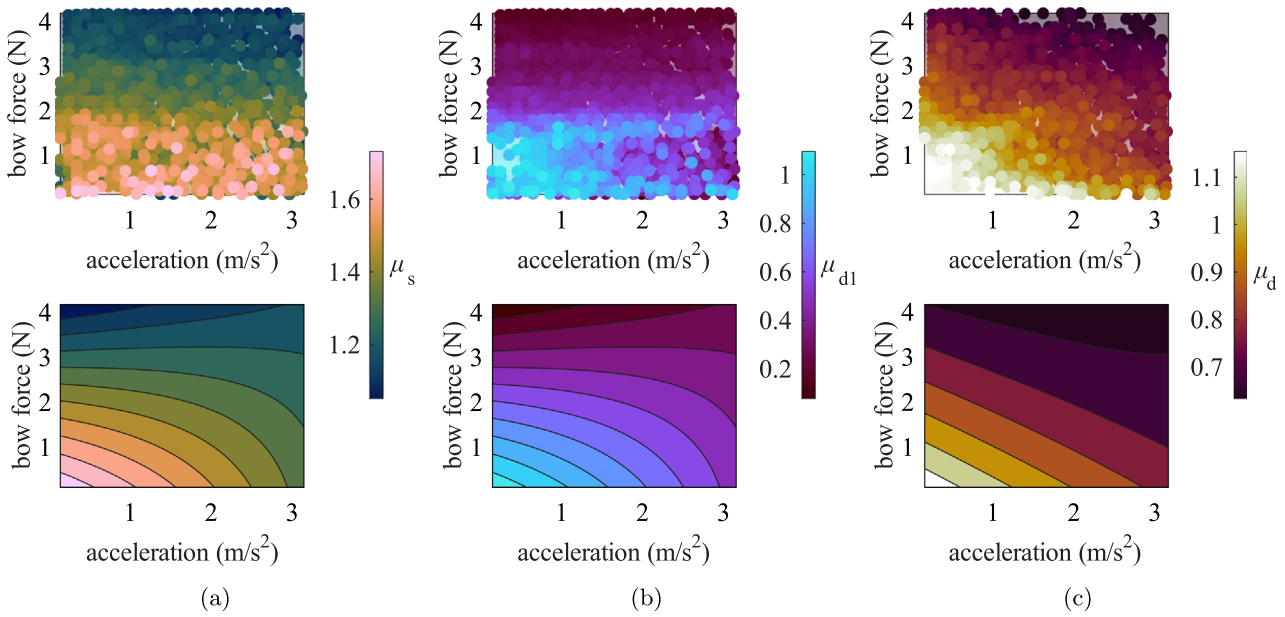

Figure 11. Measured friction coefficients obtained from the bridge force signals. The plots at the top show the measured friction coefficients, while the ones at the bottom represent the second-order polynomial fits to the measured friction coefficients using equation (5). (a) Static friction coefficient μ_s. (b) Dynamic friction coefficient at the first slip μ_{d1}. (c) Averaged "dynamic" friction coefficient μ_d, computed by taking the ratio of the average bridge force on the bowing plane and the average bridge force on the perpendicular plane over a 0.1 s time window.

this dynamic coefficient and μ_{d1}. Interestingly, the average value of μ_d is significantly higher than that of μ_{d1}, while the trends remain similar.

4.2 Guettler limits based on measured friction coefficients

In Section 4.1, we presented the measured friction coefficients and their dependence on both bow force and acceleration. While these measurements suggest an influence of bowing parameters on friction forces during transients (Fig. 11), a comprehensive theoretical model that captures this complex behaviour is currently unavailable. Therefore, in this Section, we directly incorporate the measured friction coefficients into conditions A–D for simplicity. We utilize the quadratic relationship (5) obtained by fitting the measured data to represent this dependence smoothly. It is important to note that this fitting serves solely as a visualization tool and does not represent a physical friction model.

For obtaining a closed-form solution of conditions A–D, where bow force is the sole independent variable, it is necessary to impose a constant acceleration $\hat{a}$, so that we can express the friction coefficient as $\mu_{\hat{a}} = f(F_b)$. This mathematical simplification of fixing acceleration in the inequalities for conditions A–D allows us to isolate the influence of bow force on the theoretical limits. In Figure 12, each curve illustrates the evolution of these limits with increasing bow force while assuming a constant acceleration value $\hat{a}$. This visualization highlights how the limits change shape based on the trends observed in the measured friction coefficients of Figure 11. For comparison, Figure 12 displays additional dashed lines representing limits computed with a set of fixed friction coefficients ($\mu_s = 1$, $\mu_d = 0.5$, $\mu_{d1} = 0.4$, $\mu_{d2} = 0.3$) used in Figure 10.

A complex behaviour is exhibited in response to variations in friction coefficients. At low $\hat{a}$, all curves except condition C tend to be straight lines. Condition C, however, exhibits curvature towards lower values of F_b. With increasing $\hat{a}$, all limits except C curve to the left. Condition C exhibits a distinct trend, changing curvature as $\hat{a}$ increases.

Looking back at Figure 11, we can visualise that at lower acceleration, the friction coefficients tend to exhibit higher variability with respect to bow force. Moreover, this variability becomes less pronounced at higher acceleration. This, in turn, affects the behaviour of conditions A–D when increasing $\hat{a}$. In general, at higher $\hat{a}$, the average value of the coefficient of friction decreases, leading to an increase in the limits. This behaviour is also evident in Figure 10, where the dashed lines (using lower friction coefficients) correspond to higher limits compared to the continuous lines (using higher friction coefficients).

Our observations demonstrate that the friction coefficients within the Guettler plane vary distinctively, and this needs to be an important element when predicting the playable region's limits within the Guettler diagram. The curvature observed in the limits does not reflect the typical wedge-shaped region of the experimentally obtained Guettler diagrams. However, focusing solely on the shortest transients in Figure 8, a faint resemblance can be observed between the curvature in this region and that of conditions

Table 2. Fitting coefficients obtained by applying equation (5) to the measured friction coefficients. These coefficients characterise the second-order polynomial curves used to approximate the measured friction coefficients.

	x_0	x_1	x_2	x_{12}	x_{11}	x_{22}
μ_s	1.623	−0.028	−0.112	−0.001	0.003	−0.002
μ_{d1}	1.134	−0.190	−0.243	0.068	−0.008	−0.007
μ_d	1.324	−0.186	−0.193	0.032	0.014	0.011

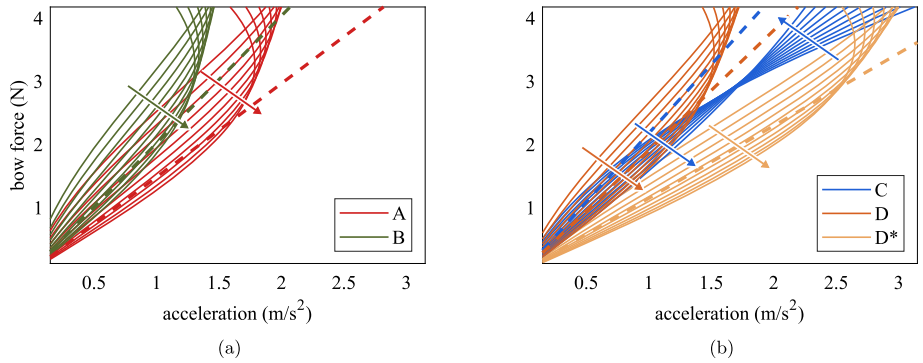

Figure 12. Guettler limits computed using friction coefficients obtained from measurements. Conditions A and B are shown in (a), while conditions C, D, and D* are displayed in (b). Ten increasing values of $\hat{a}$ were employed, ranging from 0.15 ms^{-2} to 3.15 ms^{-2}, as indicated by the arrows. For comparison, dashed lines represent limits computed with a fixed set of friction coefficients ($\mu_s = 1$, $\mu_d = 0.5$, $\mu_{d1} = 0.4$, $\mu_{d2} = 0.3$) used in Figure 10.

A, B, and D. While this is insufficient to draw definitive conclusions, it presents a potential direction for future research.

5 Discussion and conclusions

This work investigated the pre-Helmholtz transient behaviour in bowed strings using an experimental approach. The analysis focused on the playable region within the Guettler diagram, characterised by successful string attacks.

The study confirms the existence of a triangular playable region in the Guettler diagram, consistent with previous observations. Notably, the distribution of successful and unsuccessful transient times within this region appears scattered, with no clear specific area exhibiting a higher concentration of "perfect" attacks (zero transient duration). Interestingly, repeated measurements demonstrated consistent playability limits despite the inherent chaotic nature of transient times. While the higher resolution employed in this work compared to prior studies allowed for a more precise definition of the playable region boundaries, further research is needed to understand the observed clustering of "perfect" transients in later repetitions.

The observed proximity of successful and unsuccessful transient points within the playable region highlights the inherent complexity of bowed-string attacks. As similarly reported by Galluzzo [16], the detailed black and white pattern observed within the playable region likely exhibits low repeatability even under carefully controlled excitation conditions. However, the overall qualitative features, such as the position and shape of the playable region and the statistical nature of successful and unsuccessful transients, exhibit good repeatability. Therefore, comparisons between experiments, simulations, and theoretical models should primarily focus on these qualitative features.

For specific values of the relative bow-bridge distance ($\beta = 0.121$ and 0.164), a significant number of S-motion occurrences were observed. In order to exclude these motions from the analysis of the playable region, we incorporated transient time information with the oscillation rate, thereby effectively distinguishing S-motion.

Our findings align with previous numerical and experimental results, demonstrating that the playable wedge region within the Guettler diagram rotates with increasing β, and the transient times tend to be shorter within these rotated regions.

This work highlights the importance of employing friction coefficients that vary with input parameters such as bow acceleration and bow force. These findings have important implications for future research on bowed-strings. The long-term goals of this line of study involve further experimental investigations into various aspects of playability, focusing primarily on the frictional behaviour at the bow-string contact point. Additionally, comparisons between experimental data and simulations of bowed-string transients remain a key objective.

Moreover, the "speckled" nature of the experimental Guettler diagram fails to capture the capability observed in experience players, who are able to achieve perfect transients almost every time. This poses further questions on the factors influencing transient playability in bowed-string instruments. In this regard, future investigations should explore the influence of factors beyond friction coefficients.

These include the role of the vibrational response of the instrument, the transverse and torsional string damping, characteristic impedance, and inharmonicity. The current experimental setup does not allow for measurement of torsional behaviour. Future work could focus on incorporating this information in further investigations, as well as account for the ability of musicians to modulate bow force and velocity during transients.

Funding

This research was funded in whole or in part by the Austrian Science Fund (FWF) [10.55776/P34852]. For open access purposes, the authors have applied a CC BY public copyright license to any author accepted manuscript version arising from this submission.

Conflicts of interest

The authors declare no conflict of interest.

Data availability statement

The research data associated with this article are available in Zenodo with a Creative Commons Attribution 4.0 International licence, under the reference [28].

Author contributions statement

Conceptualisation, A.L.; methodology, A.L., A.M., V.C.; hardware and software A.M., A.L.; data collection, data analysis, curation and visualisation, A.L.; writing – original draft, AL.; writing – review and editing, A.L., A.M., V.C.; funding acquisition, V.C. All authors have read and agreed to the published version of the manuscript.

Statement concerning the originality of the work

The authors declare that the work is original.

References

1. J. Schelleng: The bowed string and the player, Journal of the Acoustical Society of America 53, 1 (1973) 26–41.
2. C. Raman: On the mechanical theory of the vibrations of bowed strings and of musical instruments of the violin family: with experimental verification of the results, Indian Association for the Cultivation of Science 15 (1918) 1–158.
3. R. Schumacher: Measurements of some parameters of bowing, Journal of the Acoustical Society of America 96, 4 (1994) 1985–1998.
4. E. Schoonderwaldt, K. Guettler, A. Askenfelt: An empirical investigation of bow-force limits in the Schelleng diagram, Acta Acustica united with Acustica 94, 4 (2008) 604–622.
5. P. Galluzzo: On the playability of stringed instruments, PhD thesis, University of Cambridge, 2004.
6. R. Mores: Maximum bow force revisited, Journal of the Acoustical Society of America 140, 2 (2016) 1162–1171.
7. R. Mores: Complementary empirical data on minimum bow force, Journal of the Acoustical Society of America 142, 2 (2017) 728–736.
8. T. Wofford: Study of the interaction between the musician and the instrument. Application to the playability of the cello, PhD thesis, Sorbonne Université, 2018.
9. J. Woodhouse: On the playability of violins. Part II: minimum bow force and transients, Acta Acustica united with Acustica 78, 3 (1993) 137–153.
10. H. Mansour, J. Woodhouse, G.P. Scavone: On minimum bow force for bowed strings, Acta Acustica united with Acustica 103, 2 (2017) 317–330.
11. K. Guettler: On the creation of the Helmholtz motion in bowed strings, Acta Acustica united with Acustica 88, 6 (2002) 970–985.
12. K. Guettler, A. Askenfelt: Acceptance limits for the duration of pre-Helmholtz transients in bowed string attacks, Journal of the Acoustical Society of America 101, 5 (1997) 2903–2913.
13. R. Schumacher, J. Woodhouse: The transient behaviour of models of bowed-string motion, Chaos: An Interdisciplinary Journal of Nonlinear Science 5, 3 (1995) 509–523.
14. R. Schumacher, J. Woodhouse: Computer modelling of violin playing, Contemporary Physics 36, 2 (1995) 79–92.
15. M. Demoucron: On the control of virtual violins physical modelling and control of bowed string instruments, PhD thesis, Royal Institute of Technology, Stockholm, 2008.
16. P. Galluzzo, J. Woodhouse, H. Mansour: Assessing friction laws for simulating bowed-string motion, Acta Acustica united with Acustica 103, 6 (2017) 1080–1099.
17. A. Lampis, A. Mayer, M. Pàmies-Vilà, V. Chatziioannou: Examination of the static and dynamic forces at the termination of a bowed string, Journal of the Acoustical Society of America 153, 3 supplement (2023) A198.
18. A. Mayer, A. Lampis: A versatile monochord setup: An industrial robotic arm as bowing and plucking device, Technical report, Department of Music Acoustics – Wiener Klangstil (IWK), 2024. Available at https://doi.org/10.21939/iwk-tech-report-1-2024.
19. P. Galluzzo, J. Woodhouse: High-performance bowing machine tests of bowed-string transients, Acta Acustica united with Acustica 100, 1 (2014) 139–153.
20. A. Cronhjort: A computer-controlled bowing machine, Speech Transmission Laboratory Quarterly Progress and Status Report (STL-QPSR), Department of Speech Communication and Music Acoustics, Royal Institute of Technology, Stockholm, 1992, pp. 2–3.
21. A. Mayer, M. Pàmies-Vilà, V. Chatziioannou: The universal robots real-time data exchange (RTDE) and LabView, Technical report, Department of Music Acoustics – Wiener Klangstil (IWK), 2022.
22. J. Woodhouse: Plucked guitar transients: comparison of measurements and synthesis, Acta Acustica united with Acustica 90, 5 (2004) 945–965.
23. N.J. Lynch-Aird, J. Woodhouse: Mechanical properties of nylon harp strings, Materials 10 (2017) 497.
24. C. Valette: The mechanics of vibrating strings, in: A. Hirschberg, J. Kergomard, G. Weinreich (Eds.), Mechanics of musical instruments, Springer-Verlag, Vienna and New York, 1995, pp. 115–183.
25. J. Woodhouse: Bowed string simulation using a thermal friction model, Acta Acustica united with Acustica 89, 2 (2003) 355–368.
26. J. Smith, J. Woodhouse: The tribology of rosin, Journal of the Mechanics and Physics of Solids 48, 8 (2000) 1633–1681.
27. M. McIntyre, R. Schumacher, J. Woodhouse: Aperiodicity in bowed-string motion, Acta Acustica united with Acustica 49, 1 (1981) 13–32.
28. A. Lampis: Data for experimental assessment of bowed-string transient playability limits [data set], Zenodo2024. https://doi.org/10.5281/zenodo.10946413.

Cite this article as: Lampis A. Mayer A. & Chatziioannou V. 2024. Assessing playability limits of bowed-string transients using experimental measurements. Acta Acustica, **8**, 44.